NIH-PA Author Manuscript

NIH-PA Author Manuscript

NIH-PA Author Manuscript

Near Infrared Photoacoustic Detection of Sentinel Lymph Nodes with Gold Nanobeacons

Dipanjan Pan[a,†,*], **Manojit Pramanik**[b,†], **Angana Senpan**[a], **Soumojit Ghosh**[b], **Samuel A. Wickline**[a], **Lihong V. Wang**[b,*], and **Gregory M. Lanza**[a]

[a]C-TRAIN and Division of Cardiology, Washington University School of Medicine, 4320 Forest Park Avenue, Saint Louis, MO 63108, USA

[b]Optical Imaging Laboratory, Department of Biomedical Engineering, Washington University in St. Louis, Campus Box 1097, One Brookings Drive, St. Louis, Missouri 63130, USA

Abstract

Detection of sentinel lymph node (SLN) using photoacoustic imaging is an emerging technique for noninvasive axillary staging of breast cancer. Due to the absence of intrinsic contrast inside the lymph nodes, exogenous contrast agents are used for photoacoustic detection. In this work, we have demonstrated near infrared detection of SLN with gold nanobeacons (GNB) providing the photoacoustic contrast in a rodent model. We found that size dictates the *in vivo* characteristics of these nanoparticles in SLN imaging. Larger nanobeacons with high pay loads of gold were not as efficient as smaller size nanobeacons with lower pay loads for this purpose. Colloidal GNBs were designed as a nanomedicine platform with "soft" nature that is amenable to bio-elimination, an essential feature for *in vivo* efficacy and safety. The GNBs were synthesized as lipid- or polymer-encapsulated colloidal particles incorporating tiny gold nanoparticles (2–4 nm) in three tunable sizes (90 nm, 150 nm and 290 nm). Smaller GNBs were noted trafficking through the lymphatic system and accumulating more efficiently in the lymph nodes in comparison to the bigger nanoagents. At 20 min, the GNBs reached the SLN and were no longer observed within the draining lymphatic vessel. Within one hour post injection, the contrast ratio of the lymphnodes with the surrounding blood vessels was 9:1. These findings were also supported by analytical measurements of the *ex vivo* tissue samples. Results indicate that cumulative nanoparticle deposition in lymph nodes is size dependent and that high payloads of gold, although offering greater contrast *in vitro*, may yield nanoagents with poor intradermal migration and lymphatic transport characteristics.

Keywords

Gold Nanoparticle; Near-infrared imaging; Photoacoustic imaging; Sentinel lymphnode detection; breast cancer staging

*Corresponding authors: dipanjan@wustl.edu (Nanobeacons); lhwang@biomed.wustl.edu (Photoacoustics).
†Authors: equal contribution

INTRODUCTION

In clinics, patients with breast cancer and melanoma presently undergo invasive sentinel lymph node biopsy (SLNB) to stage metastases. However, even in experienced hands the identification rates and sensitivities of this technique are less than 95% [1–3]. Moreover, SLNB can lead to seroma formation, lymphedema, sensory nerve injury, and limitation in the range of motion [4]. Therefore, an alternative noninvasive method to identify sentinel lymph nodes (SLNs) in conjunction with either minimally invasive percutaneous fine-needle biopsy (FNAB) or completely noninvasive molecular techniques will open a whole new prospect of noninvasive axillary staging for breast cancer. Noninvasive imaging modalities, e.g., magnetic resonance imaging (MRI), optical imaging, photoacoustic tomography (PAT) in combination with nanoparticle-based contrast agents show promise in improved detection of metastases. Among these, PAT is a hybrid biomedical imaging modality, which synergizes the high contrast of optical imaging with the high resolution of ultrasonic imaging. PAT has been used for various biomedical applications, such as breast cancer imaging, brain structural and functional imaging, blood-oxygenation and hemoglobin monitoring, tumor angiogenesis, and, recently molecular imaging [5–13]. The success of PAT with noninvasive SLNs mapping can be considered as a giant step towards breast cancer staging.

Noninvasive mapping of SLNs has been explored with photoacoustic (PA) imaging using various contrast agents, such as methylene blue dye, single-walled carbon nanotubes, gold nanocages, and gold nanorods [14–17]. While these approaches have seen some preliminary success in laboratory animals, it is still poorly understood how nanoparticles traverse through the lymphatic vessels and migrate into the nodes. Clearly, there is a critical unmet clinical need, and delineating this transport mechanism will further improve detection sensitivities, drug delivery efficiencies, and reduce off-target toxicity of engineered nanostructures.

We recently reported the development of **g**old **n**anobeacons (GNB_{160}s) designed for noninvasive detection of vascular biosignatures, e.g., fibrin, using photoacoustic tomography [18]. Colloidal gold nanobeacons represent a nanomedicine platform that have a "soft" nature and are amenable to bio-elimination, which are essential features for *in vivo* efficacy and safety. Ligand-directed GNB_{160}s were found to deliver ten-fold higher PA signal over blood (i.e., hemoglobin) when targeted to fibrin clots. We hypothesize that the cumulative nanoparticle accumulation in lymph nodes is size dependent and that high payloads of metal may yield nanoparticles with unsatisfactory intradermal migration and lymphatic transport characteristics.

MATERIALS AND METHODS

General Experimental Procedure

Unless otherwise listed, all solvents and reagents were purchased from Aldrich Chemical Co. (St. Louis, MO) and used as received. Anhydrous chloroform and methanol were purchased from Aldrich Chemical Co. Poly(styrene-b-acrylic acid) [19–22] (PS-*b*-PAA) was purchased from Polymer Source Inc. (Montreal, Canada). Biotinylated dipalmitoyl-phosphatidylethanolamine and high purity egg yolk phosphatidylcholine were purchased from Avanti Polar Lipids, Inc. Cholesterol and octylthiol-coated gold nanoparticles were purchased and used as received from Aldrich Chemical Co. (St. Louis, MO). Sorbitan monolaurate was purchased from Aldrich. Argon and nitrogen (Ultra High Purity: UHP, 99.99%) were used for storage of materials. The Spectra/Por membrane (Cellulose MWCO: 20 000 Da) used for dialysis was obtained from Spectrum Medical Industries, Inc. (Laguna Hills, CA).

Preparation of L-GNB$_{90}$

In a typical experimental procedure, octanethiol coated gold nanoparticles (2–4 nm, Aldrich Inc., 2% w/v) in toluene (100 mg) are suspended in sorbitan sesquioleate (4 mL, 2 mole%) and vigorously vortexed to homogeneity. The suspension was filtered through a small bed of cotton. The solvent was evaporated under reduced pressure at 45°C. The surfactant co-mixture included high purity egg yolk phosphatidylcholine (91 mole%, 380 mg), cholesterol (8 mole %, 17.39 mg), and biotinylated-dipalmitoyl phosphatidylethanolamine (1 mole%, 6.2 mg). The surfactant co-mixture was dissolved in chloroform, evaporated under reduced pressure, dried in a 40°C vacuum oven overnight, and dispersed into water by probe sonication. This suspension was combined with the gold nanoparticle-suspended sorbitan sesquioleate mixture (20% v/v), distilled deionized water (15.23 mL, 77.3% w/v), and glycerin (0.37 mL, 1.7%, w/v). The mixture was continuously processed thereafter at 20,000 PSI for 4 minutes with an S110 Microfluidics emulsifier (Microfluidics) at 4°C. The nanobeacons were dialyzed against water using a 20,000 Da MWCO cellulose membrane for a prolonged period of time and then passed through a 0.45 µm Acrodisc Syringe filter. To prevent bacterial growth the nanobeacons are stored under an argon atmosphere typically at 4°C. DLS (D_{av})/nm = 92 ± 13 nm; Zeta (ζ)/mV = −55 ± 14 mV; AFM (H_{av})/nm = 45 ± 10 nm, ICP-MS = 1.56 µg of gold /g of 20% colloidal suspension.

Preparation of P-GNB$_{290}$

In a typical experimental procedure, octane thiol coated gold nanoparticles (2–4 nm, Aldrich Inc.) in toluene were suspended in sorbitan monolaurate (1 mL, 5 mole%) and vigorously vortexed to homogeneity. The suspension was filtered through a small bed of cotton. The amphiline PS-*b*-PAA [19–22] ($Mn \times 10^{-3}$: 0.8-*b*-29.3 polydispersity index: PDI=1.18, 0.0034 mmoles, 104.0 mg, 0.5 mole%) was dissolved in a mixture of methanol and chloroform (4:1), filtered through a small bed of cotton, evaporated under reduced pressure at 50°C, dried in a 40°C vacuum oven for 6 h, and dispersed into water by probe sonication until a clear suspension was obtained. This suspension (10 mL) was combined with the gold nanoparticle-suspended polysorbate mixture (1 mL, 5 mole%), distilled deionized water (8.45 mL, 0.2 µM), and glycerin (0.45 mL). The mixture was then briefly probe sonicated at ambient temperature followed by continuous processing at 20,000 PSI (137.9 MPa) for 4 minutes with an S110 Microfluidics emulsifier (Microfluidics) at 4°C. The nanobeacons were purified by exhaustive dialysis against deionized water using 20 KDa MW CO cellulosic membrane. The nanoparticles were recovered and passed through a 0.45 µm Acrodisc Syringe filter. To slow microbial growth the colloids were stored under an argon atmosphere typically at 4°C. DLS (D_{av})/nm = 289 ± 24 nm; Zeta (ζ)/mV = −35 ± 08 mV; AFM (H_{av})/nm = 153 ± 31 nm, PDI = 0.15 ± 0.04, ICP-MS = 134 µg of gold /g of 10% colloidal suspension.

Measurements

Dynamic light scattering measurements—Instrument and method: Hydrodynamic diameter distribution and distribution averages for the GNB and controls in aqueous solutions were determined by dynamic light scattering. Hydrodynamic diameters were determined using a Brookhaven Instrument Co. (Holtsville, NY) Model Zeta Plus particle size analyzer. Measurements were made following dialysis (MWCO 10 kDa dialysis tubing, Spectrum Laboratories, Rancho Dominguez, CA) of GNB suspensions into deionized water (0.2 µM). Nanobeacons were dialyzed into water prior to analysis. Scattered light was collected at a fixed angle of 90°. A photomultiplier aperture of 400 mm was used, and the incident laser power was adjusted to obtain a photon counting rate between 200 and 300 kcps. Only measurements for which the measured and calculated baselines of the intensity autocorrelation function agreed to within +0.1% were used to calculate nanoparticle hydrodynamic diameter values. All determinations were made in multiples of five consecutive measurements.

Electrophoretic potential measurements—Instrument and method: Zeta potential (ζ) values for the gold nanobeacons were determined with a Brookhaven Instrument Co. (Holtsville, NY) model Zeta Plus zeta potential analyzer. Measurements were made following dialysis (MWCO 10 kDa dialysis tubing, Spectrum Laboratories, Rancho Dominguez, CA) of GNB suspensions into water. Data were acquired in the phase analysis light scattering (PALS) mode following solution equilibration at 25°C. Calculation of ζ from the measured nanoparticle electrophoretic mobility (μ) employed the Smoluchowski equation: $\mu = \varepsilon\zeta/\eta$, where ε and η are the dielectric constant and the absolute viscosity of the medium, respectively. Measurements of ζ were reproducible to within $\pm$ 4 mV of the mean value given by 16 determinations of 10 data accumulations.

Atomic Force Microscopy Measurements—Instrument and method: A Digital Instruments Dimension 3000 series AFM (calibration date 08/2008) and standard Veeco tapping mode silicon probes w/PtIr coating were used for scanning the samples.

In a typical methodology, aqueous suspensions of GNB samples were dried in a class 10000-clean room on a clean glass slide for 3 h. Once dried, samples were placed on the AFM and scanned. Pertinent scanning parameters were as follows: Resonant frequency (probe): 60–80 kHz; Example of tip velocity: (4 um/s for 2 um), (15 um/s for 5 um), (30 um/s for 10 um). Aspect ratio: 1:1; Lift height: 20 nm; Resolution: 512 samples/line, 256 lines. The average particle height (H_{av}) values and standard deviations were generated from the analyses of a minimum of 100 particles from three micrographs.

Inductively coupled plasma-optical emission spectroscopy (ICP-OES)—Instrument and method: The iodine and bismuth contents of cROMP were analyzed by inductively coupled plasma-optical emission spectroscopy (ICP-MS, SOP7040, Rev 9) conducted at the Bodycote, West Coast Analytical Service (WCAS), Santa Fe Springs, CA. Briefly, the samples were analyzed by a Leeman Labs Direct Reading Echelle ICP-MS, or a DRE (Direct Reading Echelle) instrument which was designed to handle sub-ppm to percent level metal concentrations. DRE consists of a 2 dimensional, high resolution Echelle grating which precisely and reliably locate any peak in the ICP spectrum.

Photoacoustic Imaging System—Instrument and method: A reflection-mode PA imaging system [23] was used for all PA experiments. A tunable Ti:sapphire laser (LT-2211A, LOTIS TII) pumped by Q-switched Nd:YAG (LS-2137, LOTIS II) laser was the light source, providing <15 ns pulse duration and a 10-Hz pulse repetition rate. A dark-field ring-shaped illumination was used [24]. The light energy on the sample surface was controlled to conform to the American National Standards Institute (ANSI) standard for maximum permissible exposure (MPE) [25]. A 5-MHz central frequency, spherically focused (2.54 cm focus length, 1.91 cm diameter active area element, and 72% bandwidth) ultrasonic transducer (V308, Panametrics-NDT) was used to acquire the generated PA signals. The signal was then amplified by a low-noise amplifier (5072PR, Panametrics-NDT), and recorded using a digital oscilloscope (TDS 5054, Tektronix) with a 50 mega-sampling rate. PA signal fluctuations due to pulse-to-pulse energy variation were compensated by signals from a photodiode (DET110, Thorlabs), which sampled the energy of each laser pulse.

A linear translation stage (XY-6060, Danaher Motion) was used for raster scanning to obtain three-dimensional (3-D) PA data. A computer controlled the stage and synchronized it with the data acquisition. To shorten the data acquisition time, a continuous scan was used without signal averaging. An A-line (A-scan) was the PA signal obtained along the depth direction at a single point. Multiple A-lines (acquired by a one-dimensional (1-D) scan) gave a two-dimensional (2-D) B-scan. A 3-D image was acquired with a 2-D scan. A 1-D depth-resolved

image was obtained by multiplying the time axis of the initial A-scan (resolved in time along the depth direction) by the speed of sound in soft tissue (~1500 m/s).

The scanning time depends on the laser pulse repetition rate (PRR), the scanning step size, and the field of view (FOV). Typical values are a scanning step size for a 1-D scan = 0.2 mm, for a 2-D scan = 0.4 mm, a laser PRR = 10 Hz, and a FOV = 24 mm × 24 mm. The acquisition time = ~25 sec for a B-scan, and = ~18 min for a 3-D image. Please note that no signal averaging was done for any of these images. The images shown here are cropped to a FOV of 17 mm×21 mm, since the outside region was not of interest. The transducer was located inside a water container with an opening of 5 cm × 5 cm at the bottom, sealed with a thin, clear membrane. The object was placed under the membrane, and ultrasonic gel was used for coupling the sound.

The laser power density on the sample surface was ~5 mJ/cm^2. For animal studies 767 nm laser was used. At 767 nm, the MPE on the skin surface by any single laser pulse is ~27 mJ/cm^2 $[20\times10^{2(\lambda-700)/1000}$ mJ/cm$^2]$, as governed by the ANSI safety standards. Therefore, we were well within the safety limit. The post-injection images were acquired within 0–5 min after the injection (denoted as 5 min post-injection image), 20–25 min after injection (denoted as 20 min post-injection image), 40–45 min after injection (denoted as 40 min post-injection image), 60–65 min after injection (denoted as 60 min post-injection image).

Animal and Drug Information—Guidelines on the care and the use of laboratory animals at Washington University in St. Louis were followed for all animal experiments. Adult Sprague Dawley rats with body weights ranging from 200–300 g were used for the *in vivo* studies. Initial anesthetization of the rat was done using a mixture of ketamine (85 mg/kg) and xylazine (15 mg/kg). The animal was maintained with 1.5–3% isoflurane in oxygen on a ventilator for approximately 2 h during the SLN imaging, which included a control image (preinjection PA signal), followed by post-injection PA image at an interval of ~20 min after injection of GNB$_{160}$s/ L-GNB$_{90}$s/ P-GNB$_{290}$s. For the noninvasive PA imaging, the hair on the region of interest of the rat was gently removed before imaging, using a commercial hair-removal lotion. A 0.15 ml of GNB$_{160}$s/ L-GNB$_{90}$s/ P-GNB$_{290}$s was intradermally injected on a left/right forepaw pad, depending on which side was imaged. PA images were acquired after the administration of GNBs. During the image acquisition, anesthesia was maintained using vaporized isoflurane (1 L/min oxygen and 0.75% isoflurane, Euthanex Corp.), and a pulse oximeter (NONIN Medical INC., 8600V) was used to monitor the vitals. If needed, 8 ml of 0.9% saline was administered to the rat for hydration. After image acquisition, the animal was euthanized by pentobarbital overdose.

RESULTS AND DISCUSSION

In the first phase of our experiment, the potential of SLN imaging with GNB$_{160}$ [D$_{av}$(DLS): 155 ± 11 nm, ICP-OES: 6120 gold/nanobeacons] was tested in a rodent model. Lymph node imaging was possible with GNB$_{160}$ (5 μM) (Fig. 3A and B), however with eight times diluted GNB$_{160}$s (~600 nM), SLNs were not visible (see supporting information for more details). The study produced mixed results with overall unsatisfactory lymph node detection sensitivity.

Our preliminary approach to resolve this issue was to increase the amount of metal within the colloidal nanobeacons. Towards this aim, we prepared **p**olymer-encapsulated **g**old **n**anobeacons (P-GNB$_{290}$s) adopting a unique approach, which is based on the self-assembly of amphiphilic di-block copolymer in aqueous media to entrap high payloads of gold. In a typical synthesis, PS-*b*-PAA [19–22] (Mn × 10^{-3}: 0.8-*b*-29.3, PDI = 1.18, 0.0033 mmoles) was dissolved in a mixture of methanol and CHCl$_3$ (4:1) and subjected to controlled evaporation under reduced pressure to generate a thin film of polymer (Fig. 1A). The thin film was dispersed in deionized water (0.2 μM) by probe sonication at ambient temperature.

Octanethiol coated AuNPs (2 w/v%) were suspended in polysorbate (sorbitan monolaureate (5 vol%) and microfluidized with a PS-*b*-PAA dispersion (0.5 vol%) to obtain the P-GNB$_{290}$ particles. The nanobeacons were purified by exhaustive dialysis against an infinite sink of nanopure water using a cellulosic dialysis membrane (20 kDa MWCO). P-GNB$_{290}$ was characterized by multiple techniques. Hydrodynamic particle sizes for the P-GNB$_{290}$ were 289 ± 24 nm observed by dynamic light scattering measurements with narrow distribution (polydispersity indexes, PDI = 0.15 ± 0.04) (Fig. 1B). The particle stability and successful amphiline-encapsulation were confirmed by the presence of negative electrophoretic potential (ζ) values. Anhydrous state morphology of the particles was observed by atomic force microscopy (AFM) studies (Fig. 1C). Gold content was determined by ICP-OES as 134 µg g^{-1}, which corresponds to 71,493 gold metal atoms per nanobeacon.

Blood (i.e., hemoglobin), which produces a strong PA signal, is a source of intrinsic contrast inside the human body. Therefore, any material that is capable of generating PA signals comparable to blood has potential to serve as an extrinsic contrast agent. The use of the near-infrared (NIR) window for PAT is well known for deep tissue imaging, although image contrast is reduced. Photoacoustic imaging of P-GNB$_{290}$ in suspension within the NIR range was promising. Fig. 2A shows P-GNB$_{290}$ (680 nM) produced a stronger PA signal than blood (λ = 767 nm). P-GNB$_{290}$s produced a peak-to-peak PA signal amplitude of 540 ± 30 mV, whereas blood produced 133 ± 7 mV. Fig. 2B shows the PA spectrum over wavelengths from 721 to 823 nm. P-GNB$_{290}$s produced a PA signal at least two times stronger than blood. The PA signal amplitude changed as the concentration of nanobeacons was varied. Fig. 2C shows how the PA signal amplitude changed for several laser wavelengths from serially diluted P-GNB$_{290}$s. It is evident that a significant PA signal was produced even at the low concentration of 10 nM, making P-GNB$_{290}$ a candidate for *in vivo* applications.

The potential of SLN imaging with the use of P-GNB$_{290}$s was explored through fore-paw injection in a rat model. Interestingly, SLN imaging with P-GNB$_{290}$s (680 nM) was unsuccessful. Fig. 3C and D show the pre- (control) and post-injection (60 min) maximum amplitude projection (MAP) [8] photoacoustic images. SLNs were dynamically monitored for three days without promising results (n = 4). This confirmed that we were not experiencing a slower, longer-lasting transport of these larger nanobeacons into the lymphatic vessels. These results led us to believe that the uptake of the P-GNB$_{290}$s in the lymphatic channels and transport to the lymph node were poor, which presumembly were correlated with the larger size and mass of these gold nanobeacons (> 250 nm).

The unsuccessful outcome prompted us to explore a smaller **l**ipid-encapsulated (~90 nm) **g**old **n**anobeacon (L-GNB$_{90}$) (Fig. 1A). Gold nanoparticles (AuNPs) were uniquely suspended within a polysorbate core matrix to avoid unfavorable interactions with the surrounding plasma proteins. In a typical procedure, octanethiol-functionalized, coated AuNPs (2 w/v% of inner matrix) were suspended in polysorbate (sorbitan monolaureate, 20 vol%) and homogenized with the surfactant mixture at 137.9 MPa for 4 min to produce L-GNB$_{90}$s. The surfactant mixture comprised mainly of phosphatidylcholine (PC) (~90 mol% of lipid constituents). Hydrodynamic particle sizes for the L-GNB$_{90}$s were 92 ± 12 nm (DLS) with narrow polydispersity indexes, PDI = 0.35 ± 0.05 (Fig. 1B). Anhydrous state particle heights were measured to be 45 ± 10 nm (Fig. 1C). Gold content was determined by ICP-OES as 1.56 µg g^{-1}, corresponding to approximately 9 gold metal atoms per L-GNB$_{90}$s.

Fig. 2 summarizes the feasibility of using L-GNB$_{90}$s as NIR contrast agents. Fig. 2A shows that L-GNB$_{90}$s (10 nM) produced a stronger PA signal than blood (λ = 767 nm). L-GNB$_{90}$s produced a peak-to-peak PA signal amplitude of 168 ± 12 mV. Interestingly, L-GNB$_{90}$s produced a stronger PA signal than blood below 795 nm wavelength but a weaker one above 800 nm. L-GNB$_{90}$s produced weaker PA signals in suspension than P-GNB$_{290}$s, presumably

due to its incorporation of much lower concentrations of gold. Although L-GNB$_{90}$s have a weaker absorption coefficient than P-GNB$_{290}$s in the NIR wavelength range, they were still considered useful for *in vivo* SLN imaging application.

The efficacy of L-GNB$_{90}$s for SLN imaging was studied in a rat model following intradermal injection of the particles, as used previously. At baseline, sagittal MAP photoacoustic image (resolution = ~500 µm, in plane) of the axillary area revealed a distinct microvasculature indicated by the red arrows (Fig. 3E). Lymph nodes were undetectable at baseline, lacking any intrinsic optical absorbers, in contradistinction to the adjacent blood vessels containing highly absorbing red blood cells. Following baseline image acquisition, L-GNB$_{90}$s (150 µL) were injected intradermally into the forepaw, and serial PA images were acquired. At 5 and 20 mins post-injection, sentinel lymphnodes were easily visualized (Fig. 3F and G). In Fig. 3F, immediately after the injection, L-GNB$_{90}$s were noted traveling through the lymphatic system (designated by the blue arrow) and accumulating in the lymphnodes. At 20 min, the L-GNB$_{90}$s had reached the SLNs and were no longer observed within the draining lymphatic vessel. Dynamic PA imaging was performed up to 1 hour post-injection, and SLNs remained visible in all the PA images (see supporting information for more details). The blood vessels and the SLN were detected with a contrast of 12 and 89, respectively (calculated from the 1 hour post-injection MAP image). The contrast is defined as the ratio of the average PA signal amplitude obtained from the blood vessel/SLN to the average background signal amplitude. Thus the contrast ratio between the SLN and the surrounding blood vessel was ~7.5:1. The signal-to-noise ratio (SNR) was 24 dB and 39 dB for blood vessels and SLN, respectively. The SNR, calculated from the raw A-line signal without any signal averaging, was defined as 20*log (peak signal amplitude/standard deviation of background). Fig. 3H illustrates the same image as in Fig. 3G, with two different color maps (green for the contribution from the nanobeacons, red for hemoglobin). Some of the nanobeacons transited into the surrounding vessels, as evident from the signal therein. An optical photograph of the excised lymph node is shown in Fig. 3K. Subsequent dissection of the lymph node revealed no outwardly visible accumulation of AuNP themselves (i.e., red color) indicating the patent integrity of the surface lipid coating.

The above experiment was successfully repeated with diluted L-GNB$_{90}$s (2.5 and 1 nM). In both cases, lymph nodes were clearly visible (Fig. 3I–J and 3M–N) in the post-injection (5 min) MAP photoacoustic image. We quantified the signal intensities and observed a ~9 times enhancement with L-GNB$_{90}$s injection, ~7.5 times enhancement with 1/4x diluted L-GNB$_{90}$s, ~5.2 times enhancement with 1/10x diluted L-GNB$_{90}$s, and ~2.6 times enhancement with GNB$_{160}$s. However, with P-GNB$_{290}$s no signal enhancement was seen after injection (average signal is ~1.01 times the pre-injection value). As a result, we concluded that SLNs mapping with P-GNB$_{290}$s was infeasible. The total gold content of the excised lymphnode specimens were analytically determined by ICP-OES as 8.74 µg g-1 and 1.99 µg g-1, (detection limit =0.02 µg g-1), for animals injected with L-GNB$_{90}$s and P-GNB$_{290}$s respectively.

CONCLUSIONS

In summary, both GNB$_{160}$s and L-GNB$_{90}$s can function as contrast agents for PA deep tissue imaging in the NIR window, with the smaller L-GNB$_{90}$s being superior for SLNs detection. Although L-GNB$_{90}$s had lower PAT contrast in suspension, *in vitro* than GNB$_{160}$s or P-GNB$_{290}$s, when injected intradermally L-GNB$_{90}$s travel quickly through the lymphatic vessels and migrate exclusively to the lymph nodes. P-GNB$_{290}$s produced strong PA signals in suspension and therefore could be beneficial for other *in vivo* application. These results suggest that cumulative nanoparticle deposition in lymph nodes is size dependent and that high payloads of gold, although offering greater contrast, may yield nanoagents with poor intradermal migration and lymphatic transport characteristics.

Supplementary Material

Refer to Web version on PubMed Central for supplementary material.

Acknowledgments

Appendix

Fig. S1–S5: UV-vis spectroscopic profile of gold nanobeacons, *in vivo* photoacoustic images of sentinel lymph nodes of rat, B-scan PA image showing the depth of the lymph nodes in rat. These materials can be found in the online version.

References

1. Krag D, Weaver D, Ashikaga T, Moffat F, Klimberg VS, Shriver C, et al. The sentinel node in breast cancer - A multicenter validation study. N Engl J Med 1998;339:941–946. [PubMed: 9753708]

2. McMasters KM, Tuttle TM, Carlson DJ, Brown CM, Noyes RD, Glaser RL, et al. Sentinel lymph node biopsy for breast cancer: A suitable alternative to routine axillary dissection in multi-institutional practice when optimal technique is used. J Clin Oncol 2000;18:2560–2566. [PubMed: 10893287]

3. Ung OA. Australasian experience and trials in sentinel lymph node biopsy: the RACS SNAC trial. Asian J Surg 2004;27:284–290. [PubMed: 15564180]

4. Purushotham AD, Upponi S, Klevesath MB, Bobrow L, Millar K, Myles JP, et al. Morbidity after sentinel lymph node biopsy in primary breast cancer: Results from a randomized controlled trial. J Clin Oncol 2005;23:4312–4321. [PubMed: 15994144]

5. Hoelen CGA, de Mul FFM, Pongers R, Dekker A. Three-dimensional photoacoustic imaging of blood vessels in tissue. Opt Lett 1998;23:648–650. [PubMed: 18084605]

6. Oraevsky, AA.; Savateeva, EV.; Solomatin, SV.; Karabutov, AA.; Andreev, VG.; Gatalica, Z., et al. Optoacoustic Imaging of Blood for Visualization and Diagnostics of Breast Cancer. In: Oraevsky, AA., editor. Proc SPIE; 2002. 2002. p. 81-94.

7. Wang XD, Pang YJ, Ku G, Xie XY, Stoica G, Wang LHV. Noninvasive laser-induced photoacoustic tomography for structural and functional in vivo imaging of the brain. Nat Biotechnol 2003;21:803–806. [PubMed: 12808463]

8. Zhang HF, Maslov K, Stoica G, Wang LHV. Functional photoacoustic microscopy for high-resolution and noninvasive in vivo imaging. Nat Biotechnol 2006;24:848–851. [PubMed: 16823374]

9. Lungu GF, Li ML, Xie XY, Wang LHV, Stoica G. In vivo imaging and characterization of hypoxia-induced neovascularization and tumor invasion. Int J Oncol 2007;30:45–54. [PubMed: 17143511]

10. Li ML, Oh JT, Xie XY, Ku G, Wang W, Li C, et al. Simultaneous molecular and hypoxia imaging of brain tumors in vivo using spectroscopic photoacoustic tomography. Proc IEEE 2008;96:481–489.

11. Wang YW, Xie XY, Wang XD, Ku G, Gill KL, O'Neal DP, et al. Photoacoustic tomography of a nanoshell contrast agent in the in vivo rat brain. Nano Lett 2004;4:1689–1692.

12. Agarwal A, Huang SW, O'Donnell M, Day KC, Day M, Kotov N, et al. Targeted gold nanorod contrast agent for prostate cancer detection by photoacoustic imaging. J Appl Phys 2007;102:064701.

13. De La Zerda A, Zavaleta C, Keren S, Vaithilingam S, Bodapati S, Liu Z, et al. Carbon nanotubes as photoacoustic molecular imaging agents in living mice. Nat Nanotechnol 2008;3:557–562. [PubMed: 18772918]

14. Song KH, Stein EW, Margenthaler JA, Wang LHV. Noninvasive photoacoustic identification of sentinel lymph nodes containing methylene blue in vivo in a rat model. J Biomed Opt 2008;13:054033. [PubMed: 19021413]

15. Pramanik M, Song KH, Swierczewska M, Green D, Sitharaman B, Wang LHV. In vivo carbon nanotube-enhanced non-invasive photoacoustic mapping of the sentinel lymph node. Phys Med Biol 2009;54:3291–3301. [PubMed: 19430111]

16. Song KH, Kim CH, Cobley CM, Xia YN, Wang LHV. Near-Infrared Gold Nanocages as a New Class of Tracers for Photoacoustic Sentinel Lymph Node Mapping on a Rat Model. Nano Lett 2009;9:183–188. [PubMed: 19072058]

17. Kim JW, Galanzha EI, Shashkov EV, Moon HM, Zharov VP. Golden carbon nanotubes as multimodal photoacoustic and photothermal high-contrast molecular agents. Nat Nanotechnol 2009;4:688–694. [PubMed: 19809462]

18. Pan D, Pramanik M, Senpan A, Yang X, Song KH, Scott MJ, et al. Molecular Photoacoustic Tomography with Colloidal Nanobeacons. Angew Chem Int Ed 2009;48:4170–4173.

19. Laruelle G, Francios J, Billon L. Self-assembly in aqueous media of amphiphilic poly acrylic acid based di-block copolymers synthesized by direct nitroxide-mediated polymerization. Macromol Rapid Commun 2004;25:1839–1844.

20. Huang HY, Kowalewski T, Remsen EE, Gertzmann R, Wooley KL. Hydrogel-coated glassy nanospheres: A novel method for the synthesis of shell cross-linked knedels. J Am Chem Soc 1997;119:11653–11659.

21. Wu J, Eisenberg A. Proton diffusion across membranes of vesicles of poly(styrene-bacrylic acid) diblock copolymers. J Am Chem Soc 2006;128:2880–2884. [PubMed: 16506766]

22. Xu J, Sun G, Rossin R, Hagooly A, Li Z, Fukukawa K, et al. Labeling of Polymer Nanostructures for Medical Imaging: Importance of charge density, spacer length, and crosslinking extents. Macromolecules 2007;40:2971–2973. [PubMed: 18779874]

23. Song KH, Wang LHV. Deep reflection-mode photoacoustic imaging of biological tissue. J Biomed Opt 2007;12:060503. [PubMed: 18163798]

24. Maslov K, Stoica G, Wang LVH. In vivo dark-field reflection-mode photoacoustic microscopy. Optics Lett 2005;30:625–627.

25. Laser Institute of America. American National Standard for Safe Use of Lasers ANSI Z136.1–2000. New York, NY: American National Standards Institute, Inc.; 2000.
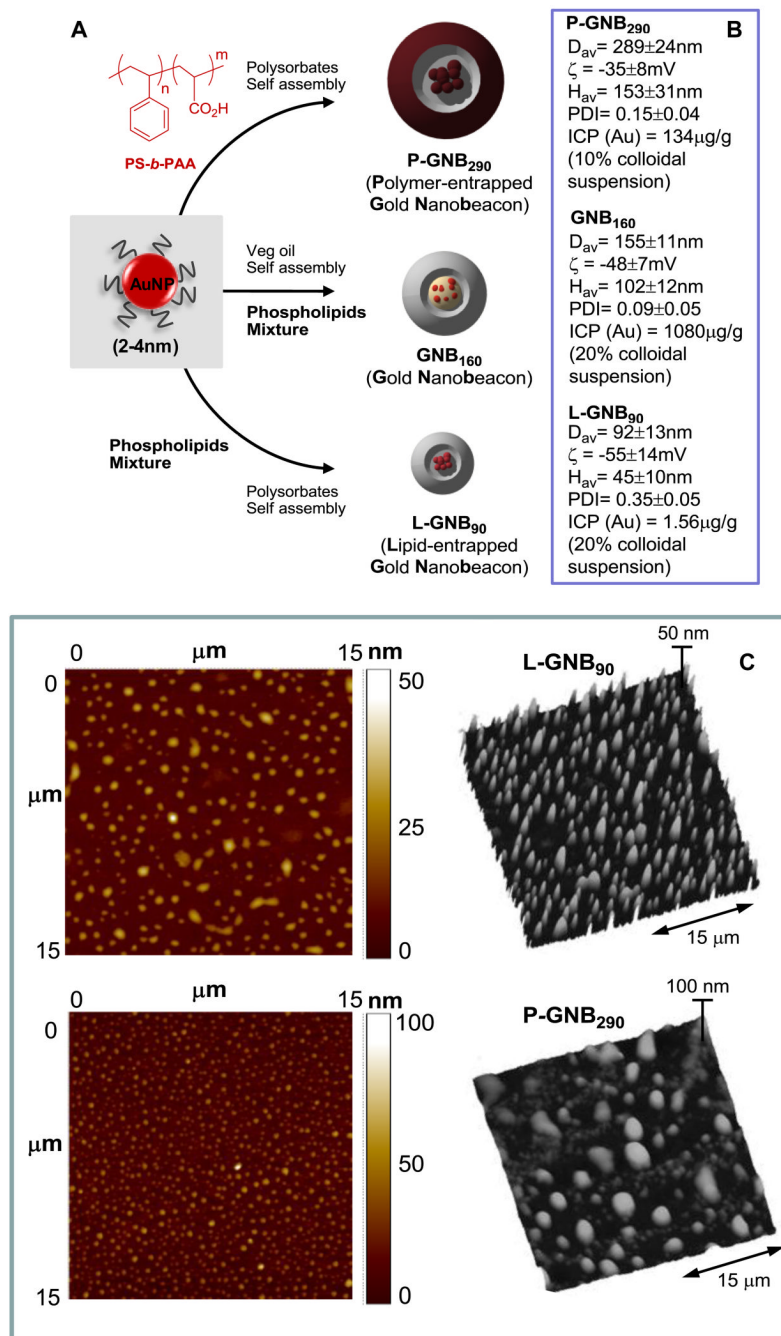
Fig. 1.
A. Synthesis of GNBs. B. Physico-chemical characterization. C. Anhydrous state AFM images (drop-deposited on glass). [D_{av}= Number averaged (DLS); ζ= electrophoretic (zeta) potential; H_{av}= average height (AFM); PDI= polydispersity index (DLS); ICP (Au)= analytical gold content (ICP-OES)., height scale expressed in nm].
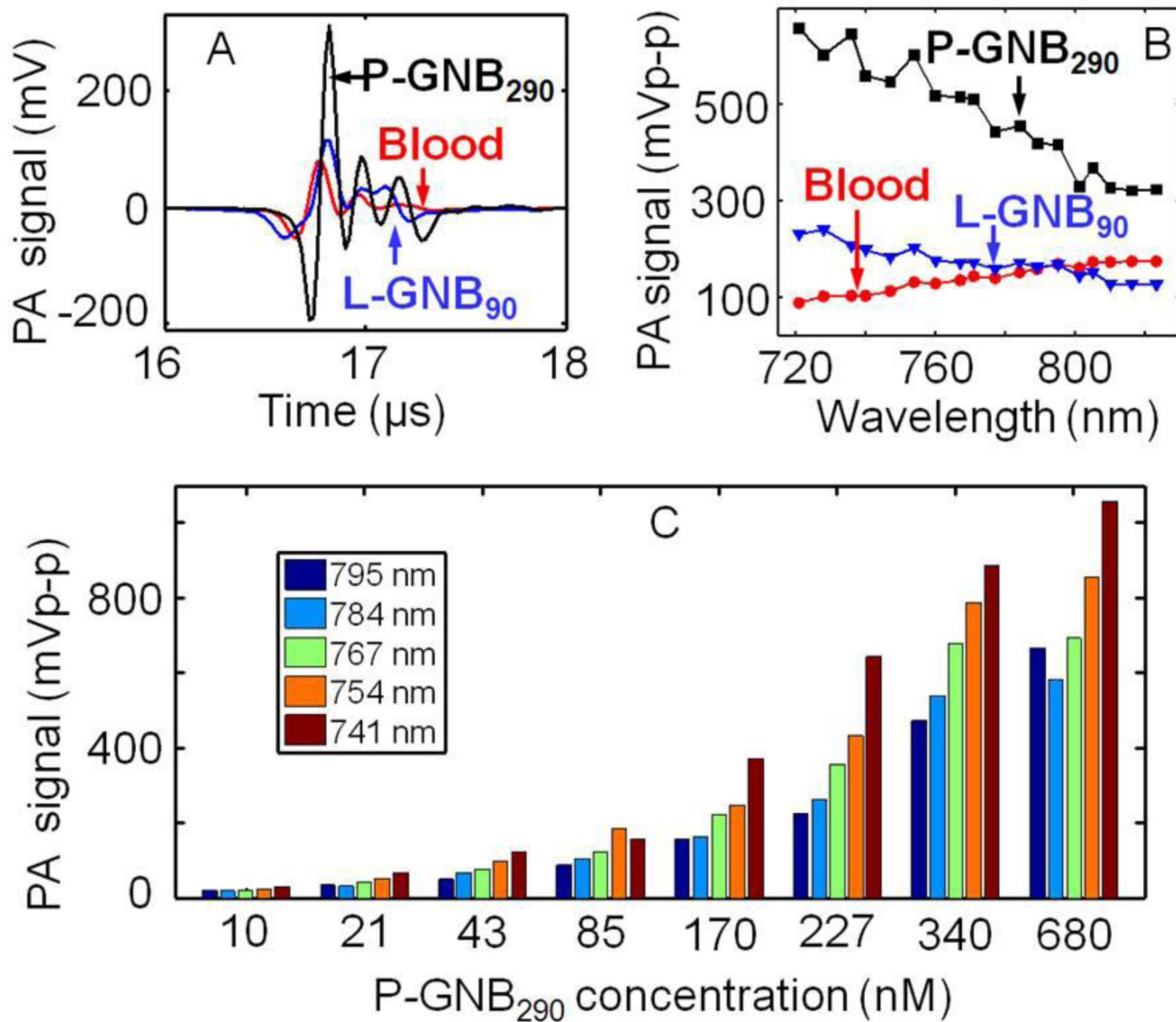
Fig. 2.
A. Photoacoustic (PA) signals generated from a tube (Silastic® laboratory tubing, Dow Corning Corp., I.D. 300 µm, O.D. 640 µm) filled with P-GNB$_{290}$s (680 nM), L-GNB$_{90}$s (10 nM), and blood at $\lambda = 767$ nm. B. PA spectrum of P-GNB$_{290}$s, L-GNB$_{90}$s, and blood. C. PA signal of serially diluted P-GNB$_{290}$s at various wavelengths.
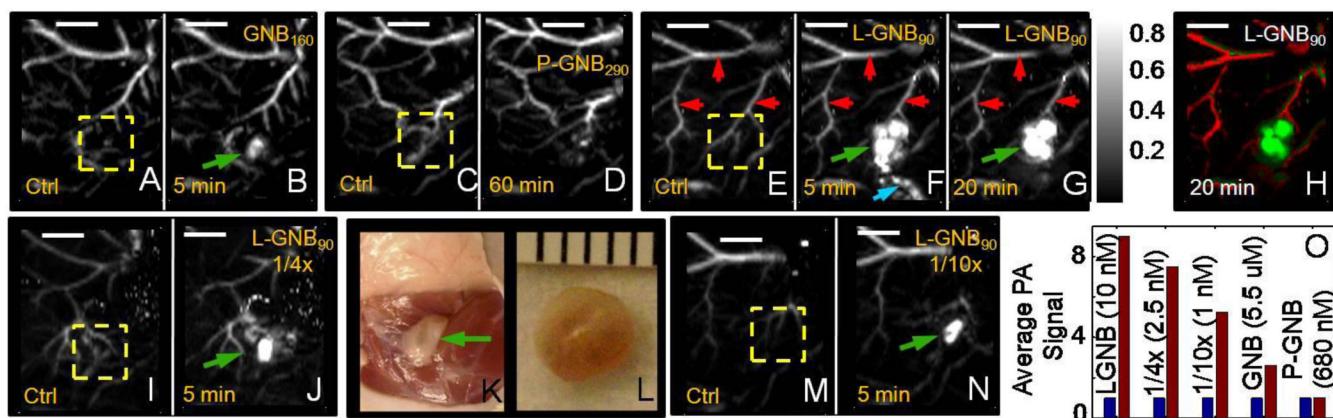
Fig. 3.
In vivo noninvasive photoacoustic imaging of sentinel lymph nodes in rat ($\lambda = 767$ nm). (A–J, M–N) Scale bar is 5 mm. 150 µL of nanobeacons were injected intradermally in all the cases.
GNB_{160}: A. Control PA image. B. 5 min post-injection image of GNB_{160}s (5 µM).
$P\text{-}GNB_{290}$: C. Control PA image. D. Lymph node is not visible in a 60 min post-injection image of $P\text{-}GNB_{290}$s (680 nM).
$L\text{-}GNB_{90}$: E. Sagittal maximum amplitude projection (MAP) [8] pre-injection control image: Bright parts represent optical absorption from blood vessels, marked with red arrows. F. PA image (MAP) acquired 5 min after $L\text{-}GNB_{90}$ injection (10 nM). SLNs are clearly visible, marked with green arrow. Lymphatic vessel is also visible, marked with blue arrow. G. 20 min post-injection PA image. H. Same as G with two different color spaces showing the blood vessel as well as the SLNs. I. Control PA image. J. 5 min post-injection image of 4 times diluted $L\text{-}GNB_{90}$s (2.5 nM). K. Digital optical photograph of the rat with the skin removed after PA imaging. Lymph node area is shown with green arrow. L. Excised lymph node. Smallest tick: 1 mm. M. Control PA image. N. 5 min post-injection image of 10 times diluted $L\text{-}GNB_{90}$s (1 nM). O. Average PA signal from the ROI (marked as yellow dotted square in all the pre-injection or control images, 3A, C, E, I, M). Blue represents pre-injection and brown represents post-injection. Images are normalized by pre-injection signal.